PHOTONICS Research

Improved generation of correlated photon pairs from monolayer WS₂ based on bound states in the continuum

Tiecheng Wang, Zhixin Li, and Xiangdong Zhang*

Beijing Key Laboratory of Nanophotonics & Ultrafine Optoelectronic Systems, School of Physics, Beijing Institute of Technology, Beijing 100081, China
Corresponding author: zhangxd@bit.edu.cn

Entangled photons are the fundamental resource in quantum information processing. How to produce them efficiently has always been a matter of concern. Here we propose a new way to produce correlated photons efficiently from monolayer WS₂ based on bound states in the continuum (BICs). The BICs of radiation modes in the monolayer WS₂ are realized by designing the photonic crystal slab-WS₂-slab structure. The generation efficiency of correlated photon pairs from such a structure has been studied by using a rigorous quantum model of spontaneous parametric down-conversion with the plane wave expansion method. It is found that the generation efficiency of correlated photon pairs is greatly improved if the signal and idler fields are located at the BICs determined by the inverse scattering matrix of the structure. This is in contrast to the parametric down-conversion process for the enhanced generation of nonlinear waves if the pump field is located at the BICs determined by the scattering matrix of the structure. The generation rate of the correlated photon pairs can be improved by 7 orders of magnitude in some designed structures. The generated quantum signals are sensitive to the wavelength and exhibit narrowed relative line width, which is very beneficial for quantum information processing.   © 2019 Chinese Laser Press

https://doi.org/10.1364/PRJ.7.000341

1. INTRODUCTION

In the past two decades, there has been a great deal of interest in studying how to produce entangled photon pairs, because they play a crucial role in quantum information processing [1–3]. Many methods to produce such resources have been developed [4–7]. A popular approach to generating entangled photon pairs is based on the nonlinear process of parametric down-conversion in naturally birefringent nonlinear crystals such as β-barium borate (BBO) [8]. Other mechanisms, such as using quantum dots, quasi-phase-matching in photonic crystals, and periodically poled materials, have also been proposed [9–18].

On the other hand, nonlinear optical properties of monolayer transition metal dichalcogenides (TMDC) have attracted much attention in recent years because monolayer TMDC as two-dimensional systems have ultra-high second-order nonlinear susceptibility [19–22]. For example, some investigations have shown that the value of the effective second-order nonlinear susceptibility for the monolayer WS₂ is 3 orders of magnitude larger than the values usually reported for other nonlinear bulk crystals [23]. The question is whether the

ultra-high second-order nonlinear susceptibility in the monolayer TMDC can be used to produce entangled photons efficiently. In fact, such an idea is constrained by weak interactions between monolayer TMDC and light due to the single atom thickness of the sample. The weak interactions block efficient generation of nonlinear effects.

Fortunately, some methods to improve the interaction between monolayer materials and electromagnetic (EM) waves have been proposed [24–27]. For example, bound states in the continuum (BICs) can be utilized to improve this interaction [28,29]. Analogous to the localized electrons with energy larger than their potential barriers, light BICs have been realized in recent years [30–34]. The BICs are known as embedded trapped modes, which correspond to discrete eigenvalues co-existing with extended modes of a continuous spectrum. They have been shown to exist in the dielectric gratings, waveguide structures, the surface of the object, photonic crystal slabs, and some open subwavelength nanostructures [35–40]. Recently, it has been demonstrated that nonlinear effects can be improved greatly using these BICs [41].

Motivated by these investigations, in this work we explore the possibility to improve the generation rate of correlated

photon pairs based on the BICs. In order to calculate this generation rate in our model including a photonic crystal slab, we extend the previous quantum theory of spontaneous parametric down-conversion (SPDC) by using a plane wave expansion method for the first time to our knowledge. We find that photon-pair generation is enhanced if the signal and idler fields are located at the resonant state determined by the inverse scattering matrix of the structure and the generated fields possess a narrowed relative line width and directivity. It is noted that we do not perform the comparison between our monolayer source of WS$_2$ with those SPDC sources, such as periodically poled lithium niobate (PPLN) waveguides and periodically poled KTiOPO$_4$ (PPKTP) crystal. This is because it is not suitable for comparing the source of the monolayer atom with those of bulk SPDC sources. However, we compare the case based on the BICs with those of bare monolayers.

2. THEORY AND METHOD

We consider a three-layer structure consisting of a photonic crystal slab, a monolayer WS$_2$, and a dielectric slab as shown in Figs. 1(a) and 1(b). The monolayer WS$_2$ is put at the interface between the photonic crystal slab and the dielectric slab. The photonic crystal slab consists of a square lattice of air holes introduced into a high-index dielectric medium, and the corresponding lattice constant is denoted by l. The thickness, relative permittivity, and relative permeability of this high-index medium are denoted by d_1, ε_p, and μ_p, respectively. The thickness, relative permittivity, and relative permeability of the dielectric slab are represented by d_2, ε_s, and μ_s, respectively. The thickness, relative permittivity, relative permeability, and second-order susceptibility of the monolayer WS$_2$ are described by d_w, ε_w, μ_w, and $\chi^{(2)}$. All these materials are taken to be nonmagnetic. The photonic crystal slab and dielectric slab are taken to be linear in order to investigate the nonlinear effect of monolayer WS$_2$. As one component of TMDC monolayers, the relative permittivity of monolayers WS$_2$ can be calculated by the permittivity of TMDC monolayer $\varepsilon_{\mathrm{TMDC}}$, which is equal to a superposition of N Lorentzian functions [42,43],
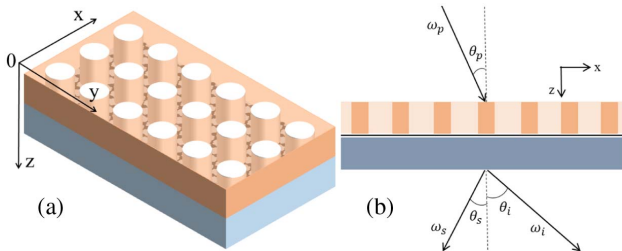

Fig. 1. (a) Diagram of the photonic crystal slab-monolayer WS$_2$-slab. The air holes are arranged in a square lattice with lattice constant l and the radius of the holes is r. The thicknesses of the photonic crystal slab and dielectric slab are denoted by d_1 and d_2, and the monolayer WS$_2$ is put at the interface between the photonic crystal slab and the dielectric slab. (b) Schematic of the photon-pair generation process in the three-layer structure. The pump beam with frequency ω_p and angle θ_p is incident on the three-layer structure, and due to the second-order nonlinear effect of the monolayer WS$_2$, the signal field with frequency ω_s and angle θ_s and the idler field with frequency ω_i and angle θ_i are generated.

$\varepsilon_{\mathrm{TMDC}} = 1 + \sum_{k=1}^{N} \frac{f_k}{\omega_k^2 - \omega^2 - i\omega\gamma_k}$, where ω is the angular frequency of the EM wave; f_k, ω_k, and γ_k represent the oscillator strength, resonance frequency, and spectral width of the kth oscillator, respectively; and the values of these model parameters are provided in Ref. [44].

A. Theory for the Spontaneous Parametric Down-Conversion in the Photonic Crystal Slab-Monolayer WS$_2$-Slab Structure

In contrast to the graphene, TMDC monolayers are noncentrosymmetric and therefore the second-order nonlinear effect is allowed. Based on the symmetry properties of their space group D_{3h}, it can be shown that the structure of their quadratical susceptibility tensor $\chi^{(2)}$ yields only one independent and nonvanishing component [4,5]:

$$\chi^{(2)} = \chi^{(2)}_{yyy} = -\chi^{(2)}_{yxx} = -\chi^{(2)}_{xyx} = -\chi^{(2)}_{xxy}, \qquad (1)$$

where x represents the zigzag direction of the monolayer and y is the orthogonal armchair direction. According to Ref. [23], the effective thickness of the monolayer WS$_2$ is taken as $d_w = 0.618$ nm. Figure 1(b) shows the process of photon-pair generation in the three-layer structure. When a pump field with the angular frequency ω_p is incident on the structure, the signal and idler fields with angular frequencies ω_s and ω_i, respectively, are generated simultaneously due to the second-order nonlinear effect of the monolayer WS$_2$, the incident angle of the pump wave is denoted by θ_p, and the irradiated angles of the signal and idler fields are taken as θ_s and θ_i. The nonlinear interaction in the three-layer structure is described by a Hamiltonian $H_{\mathrm{int}}(t)$:

$$H_{\mathrm{int}}(t) = \varepsilon_0 \int \mathrm{d}\vec{r} \sum_{\alpha,\beta,\gamma} [\chi^{(2)}_{\alpha\beta\gamma} E^+_{p,\alpha}(\vec{r}, t)\hat{E}^-_{s,\beta}(\vec{r}, t)\hat{E}^-_{i,\gamma}(\vec{r}, t) + \mathrm{H.c.}],$$

$$(2)$$

where ε_0 is the permittivity of air and $\chi^{(2)}_{\alpha\beta\gamma}$ represent the components of susceptibility tensor $\chi^{(2)}$ of the monolayer WS$_2$. Here α, β, and γ denote the direction (x or y), $E^+_{p,\alpha}(\vec{r}, t)$ is the positive frequency electric field for the classical strong pump wave at the monolayer WS$_2$, and $\hat{E}^+_{s,\beta}(\vec{r}, t)$ and $\hat{E}^+_{i,\gamma}(\vec{r}, t)$ denote the corresponding electric field operators for the generated photons with frequencies ω_s and ω_i. $E^-_{p,\alpha}(\vec{r}, t)$, $\hat{E}^-_{s,\beta}(\vec{r}, t)$, and $\hat{E}^-_{i,\gamma}(\vec{r}, t)$ denote the corresponding negative frequency electric fields, which are the conjugated terms of the positive frequency fields. H.c. stands for a Hermitian conjugated term.

The plane-wave expansion method is utilized to study the photon-pair generation [45]. Because of the periodicity of the three-layer structure, the pump field can be expanded in plane waves as

$$E^+_{p,\alpha}(\vec{r}, t) = \sum_{mn} [E_{pFmn,\alpha} \exp(i\beta_{pmn}z) + E_{pBmn,\alpha} \exp(-i\beta_{pmn}z)]$$

$$\times \exp[i(k_{pmnx}x + k_{pmny}y) - i\omega_p t]$$

$$= \sum_{mn} E^+_{pmn,\alpha}(z, \omega_p) \exp[i(k_{pmnx}x + k_{pmny}y) - i\omega_p t],$$

$$(3)$$

$$\beta_{pmn} = \sqrt{k_p^2 - k_{pmnx}^2 - k_{pmny}^2}, \qquad k_p = \omega_p n(\omega_p)/c, \qquad (4)$$

where $(k_{pmnx}, k_{pmny}) = (k_{px}, k_{py}) + m\vec{b}_1 + n\vec{b}_2$ is the Bragg wave vector of the pump field in the x–y plane, (k_{px}, k_{py}) is the reduced wave vector that lies in the surface Brillouin zone, $\vec{b}_1$ and $\vec{b}_2$ represent the reciprocal lattice vector, the corresponding wave vector along the z direction is denoted by β_{pmn}, and the magnitude of the wave vector is marked by k_p. $n(\omega_p)$ stands for the refractive index of the monolayer WS_2 for the pump field with frequency ω_p, and c denotes the velocity of light in the air. $E_{pFmn,\alpha}$ and $E_{pBmn,\alpha}$ represent the amplitude for the downward and upward propagating parts of the pump field. The electric field operators $\hat{E}_{v,\alpha}^{+}(\vec{r}, t)$ with the frequency ω_v and polarization α for the signal ($v = s$) and idler ($v = i$) fields in the monolayer WS_2 can be also expanded in plane waves [46,11]:

$$\begin{pmatrix} \hat{a}_{vF}^4 \\ \hat{a}_{vB}^0 \end{pmatrix} = \begin{pmatrix} Q_{\text{I}} & Q_{\text{II}} \\ Q_{\text{III}} & Q_{\text{IV}} \end{pmatrix} \begin{pmatrix} \hat{a}_{vF}^0 \\ \hat{a}_{vB}^4 \end{pmatrix} = Q \begin{pmatrix} \hat{a}_{vF}^0 \\ \hat{a}_{vB}^4 \end{pmatrix}, \quad \textbf{(8a)}$$

$$\begin{pmatrix} \hat{a}_{vF}^2 \\ \hat{a}_{vB}^2 \end{pmatrix} = \begin{pmatrix} T_{\text{I}}^{1,2} & T_{\text{II}}^{1,2} \\ T_{\text{III}}^{1,2} & T_{\text{IV}}^{1,2} \end{pmatrix} \begin{pmatrix} \hat{a}_{vF}^0 \\ \hat{a}_{vB}^0 \end{pmatrix} = T^{1,2} \begin{pmatrix} \hat{a}_{vF}^0 \\ \hat{a}_{vB}^0 \end{pmatrix}, \quad \textbf{(8b)}$$

where the submatrices Q_η ($\eta =$ I, II, III, IV) of scattering matrix Q [45,47] and submatrices $T_\kappa^{1,2}$ ($\kappa =$ I, II, III, IV) of transfer matrix $T^{1,2}$ [48] can be obtained by the boundary conditions, and the superscripts 1, 2 in the transfer matrixes stand for the slices consisting of the photonic crystal slab and monolayer WS_2. Based on Eq. (8), the operator matrixes $\hat{a}_{vF}^2$ and $\hat{a}_{vB}^2$ in the monolayer WS_2 can be expressed in terms of the operator matrixes $\hat{a}_{vF}^4$ and $\hat{a}_{vB}^0$ outside the structure as

$$\begin{pmatrix} \hat{a}_{vF}^2 \\ \hat{a}_{vB}^2 \end{pmatrix} = \begin{pmatrix} T_{\text{I}} & T_{\text{II}} \\ T_{\text{III}} & T_{\text{IV}} \end{pmatrix} \begin{pmatrix} -(Q_{\text{III}} - Q_{\text{IV}}Q_{\text{II}}^{-1}Q_{\text{I}})^{-1}Q_{\text{IV}}Q_{\text{II}}^{-1} & (Q_{\text{III}} - Q_{\text{IV}}Q_{\text{II}}^{-1}Q_{\text{I}})^{-1} \\ 0 & 1 \end{pmatrix} \begin{pmatrix} \hat{a}_{vF}^4 \\ \hat{a}_{vB}^0 \end{pmatrix} = \begin{pmatrix} F_{v11} & F_{v12} \\ F_{v21} & F_{v22} \end{pmatrix} \begin{pmatrix} \hat{a}_{vF}^4 \\ \hat{a}_{vB}^0 \end{pmatrix}. \quad \textbf{(9)}$$

It can be easily verified that the following equation holds:

$$Q^{-1*} = \begin{pmatrix} Q_{\text{I}}^{-1*} & Q_{\text{II}}^{-1*} \\ Q_{\text{III}}^{-1*} & Q_{\text{IV}}^{-1*} \end{pmatrix} = \begin{pmatrix} Q_{\text{I}} & Q_{\text{II}} \\ Q_{\text{III}} & Q_{\text{IV}} \end{pmatrix}^{-1*} = \begin{pmatrix} -(Q_{\text{III}} - Q_{\text{IV}}Q_{\text{II}}^{-1}Q_{\text{I}})^{-1}Q_{\text{IV}}Q_{\text{II}}^{-1} & (Q_{\text{III}} - Q_{\text{IV}}Q_{\text{II}}^{-1}Q_{\text{I}})^{-1} \\ Q_{\text{II}}^{-1} + Q_{\text{II}}^{-1}Q_{\text{I}}(Q_{\text{III}} - Q_{\text{IV}}Q_{\text{II}}^{-1}Q_{\text{I}})^{-1}Q_{\text{IV}}Q_{\text{II}}^{-1} & -Q_{\text{II}}^{-1}Q_{\text{I}}(Q_{\text{III}} - Q_{\text{IV}}Q_{\text{II}}^{-1}Q_{\text{I}})^{-1} \end{pmatrix}^*. \quad \textbf{(10)}$$

$$\hat{E}_{v,\alpha}^{-}(\vec{r}, t)$$
$$= \int_0^\infty d\omega_v \sum_{mn} G_{vmn}[\hat{a}_{vFmn,\alpha}^2 \exp(i\beta_{vmn}z)$$
$$+ \hat{a}_{vBmn,\alpha}^2 \exp(-i\beta_{vmn}z)] \exp[i(k_{vmnx}x + k_{vmny}y) - i\omega_v t]$$
$$= \int_0^\infty d\omega_v \sum_{mn} \hat{E}_{vmn,\alpha}^-(z, \omega_v) \exp[i(k_{vmnx}x + k_{vmny}y) - i\omega_v t],$$

$$\textbf{(5)}$$

$$G_{vmn} = \sqrt{\frac{\varepsilon_0 \hbar \omega^2 \varepsilon_I(\omega_v)}{8\pi \beta_{vmn}^I \beta_{vmn}^2}}, \quad \textbf{(6)}$$

$$\beta_{vmn} = \sqrt{k_v^2 - k_{vmnx}^2 - k_{vmny}^2}, \qquad k_v = \frac{\omega_v}{c}n(\omega_v). \quad \textbf{(7)}$$

Here $\hbar$ is the reduced Planck constant, B denotes the area of the transverse profile of the beam, and β_{vmn}^I and $\varepsilon_I(\omega_v)$ are the imaginary parts of β_{vmn} and $\varepsilon(\omega_v)$, respectively. $\hat{a}_{vFmn,\alpha}^2$ and $\hat{a}_{vBmn,\alpha}^2$ are the annihilation operators for the generated field in the monolayer WS_2, and the superscript 2 represents that the monolayer WS_2 is located at the second layer; these operators can be written in the matrix forms $\hat{a}_{vF}^2 = (\cdots \hat{a}_{vFmn,x}^2, \hat{a}_{vFmn,y}^2 \cdots)^T$ and $\hat{a}_{vB}^2 = (\cdots \hat{a}_{vBmn,x}^2, \hat{a}_{vBmn,y}^2 \cdots)^T$. In a similar way, the annihilation operators for the generated field up (down) the three-layer structure are denoted by $\hat{a}_{vFmn,\alpha}^0$ and $\hat{a}_{vBmn,\alpha}^0$ ($\hat{a}_{vFmn,\alpha}^4$ and $\hat{a}_{vBmn,\alpha}^4$); these operators can also be written in the matrix forms $\hat{a}_{vF}^l = (\cdots \hat{a}_{vFmn,x}^l, \hat{a}_{vFmn,y}^l \cdots)^T$ and $\hat{a}_{vB}^l = (\cdots \hat{a}_{vBmn,x}^l, \hat{a}_{vBmn,y}^l \cdots)^T$ ($l = 0, 4$). These operators can be expressed as

Combining Eqs. (9) and (10), we find that parts of the matrices F_{v11}^*, F_{v12}^*, F_{v21}^*, and F_{v22}^*, which connect the creation operators in the WS_2 to the creation operators outside the structure, are constructed by parts of the inverse scattering matrix Q^{-1*}.

In classical scattering problems, the transmission (t), reflection (r), and absorption (a) can be calculated by the scattering matrix in the following method. Assuming that the wave $\sum_{mn} E_{Fmn,\alpha}^{in} \exp(i\beta_{mn}z) \exp[i(k_{mnx}x + k_{mny}y) - i\omega t]$ is incident on the system, the transmitted wave $\sum_{mn} E_{Fmn,\alpha}^{tr} \exp(i\beta_{mn}z) \cdot \exp[i(k_{mnx}x + k_{mny}y) - i\omega t]$ and reflected wave $\sum_{mn} E_{Bmn,\alpha}^{rf} \cdot \exp(-i\beta_{mn}z) \exp[i(k_{mnx}x + k_{mny}y) - i\omega t]$ can be calculated by the scattering matrix Q as

$$E_{Fmn,\alpha}^{tr} = \sum_{pq\beta} Q_{\text{I},mn\alpha,pq\beta} E_{Fpq,\beta}^{in}, \quad \textbf{(11a)}$$

$$E_{Bmn,\alpha}^{rf} = \sum_{pq\beta} Q_{\text{III},mn\alpha,pq\beta} E_{Fpq,\beta}^{in}. \quad \textbf{(11b)}$$

Based on the calculated SH fields in Eq. (11), the electric field intensities of the transmitted $[I_{tr}(2\omega)]$ and reflected $[I_{rf}(2\omega)]$ SH fields radiated from the three-layer structure can be calculated by

$$I_{tr}(2\omega) = \frac{1}{2}\varepsilon_0 \sum_{\alpha, mn} [E_{3,\alpha,mn}^+(2\omega)][E_{3,\alpha,mn}^+(2\omega)]^*, \quad \textbf{(12a)}$$

$$I_{rf}(2\omega) = \frac{1}{2}\varepsilon_0 \sum_{\alpha, mn} [E_{0,\alpha,mn}^-(2\omega)][E_{0,\alpha,mn}^-(2\omega)]^*, \quad \textbf{(12b)}$$

$$I_{in}(\omega) = \frac{1}{2}\varepsilon_0 \sum_{\alpha, mn} [E_{in,\alpha,mn}^+(\omega)][E_{in,\alpha,mn}^+(\omega)]^*. \quad \textbf{(12c)}$$

Thus, the conversion efficiencies for the SHG fields can be obtained as

$$F = \frac{I_{tr}(2\omega) + I_{rf}(2\omega)}{I_{in}(\omega)}. \tag{13}$$

And the transmission t (reflection r) is defined as the ratio of the flux of the transmitted (reflected) wave to the flux of the incident wave and can be expressed as

$$t = \frac{\sum_{mna} E_{Fmn,\alpha}^{tr} E_{Fmn,\alpha}^{tr*} \beta_{mn}}{\sum_{pq\alpha} E_{Fpq,\alpha}^{in} E_{Fpq,\alpha}^{in*} \beta_{pq}}, \tag{14a}$$

$$r = \frac{\sum_{mna} E_{Bmn,\alpha}^{rf} E_{Bmn,\alpha}^{rf*} \beta_{mn}}{\sum_{pq\alpha} E_{Fpq,\alpha}^{in} E_{Fpq,\alpha}^{in*} \beta_{pq}}. \tag{14b}$$

According to the energy conservation, the absorption a is

$$a = 1 - t - r. \tag{14c}$$

The transmission t', reflection r', and absorption a' can also be defined as the expressions of t, r, and a in Eq. (14) except that the transmitted wave amplitude $E_{Fmn,\alpha}^{tr}$ and reflected wave amplitude $E_{Fmn,\alpha}^{rf}$ calculated by the scattering matrixes Q_{I} and Q_{III} are replaced by the corresponding wave amplitudes calculated by the inverse scattering matrixes Q_{I}^{-1*} and Q_{III}^{-1*}.

After getting the transmission t (t'), reflection r (r'), absorption a (a'), and the scattering (inverse) matrixes, we can get the corresponding electric field $\mathbf{E}$ ($\mathbf{E}'$) distribution in the three-layer structure. Here we omit the effect of the photon-pair generation on the electric field distribution, because the second-order nonlinear effect is so weak compared with the fundamental frequency field. In the next part of this work, we denote the electric field $\mathbf{E}$ ($\mathbf{E}'$) at the WS$_2$ and $\mathbf{E}_{\text{W}}$ ($\mathbf{E}'_{\text{W}}$) at $x = 0$ and $y = 0$. Inserting Eqs. (3) and (5) into Eq. (2), we can get the following expression by using the transverse Fourier transformation:

$$H_{\text{int}}(t) = \varepsilon_0 B \sqrt{2\pi} \int_0^\infty d\omega_s \int_0^\infty d\omega_i \int dz \chi_{\alpha\beta\gamma}^{(2)}$$
$$\times \sum_{mn,\,ot,\,rs} \delta(k_{pmnx} - k_{sotx} - k_{irsx})\delta(k_{pmny} - k_{soty} - k_{irsy})$$
$$\times E_{pmn,\alpha}^+(z, \omega_p)\hat{E}_{sot,\beta}^-(z, \omega_s)\hat{E}_{irs,\gamma}^-(z, \omega_i)$$
$$\times \exp[-i(\omega_p - \omega_s - \omega_i)] + \text{H.c.}. \tag{15}$$

From Eq. (15), the transverse wave vectors of the pump, signal, and idler fields satisfy the following relations:

$$k_{pmnx} - k_{sotx} - k_{irsx} = 0, \tag{16a}$$

$$k_{pmny} - k_{soty} - k_{irsy} = 0. \tag{16b}$$

B. Theory for the Generation of Correlated Photon Pairs Based on Bound States in the Continuum

The output state $|\psi\rangle_{s,\beta,i,\gamma}^{\text{out}}$ of signal and idler fields can be obtained by the Schrödinger equation with the assumption of the incident vacuum state $|\text{vac}\rangle$; furthermore, we expand it to the first order in nonlinear perturbation as

$$|\psi\rangle_{s,\beta,i,\gamma}^{\text{out}} = \exp\left[-\frac{i}{\hbar}\int_{-\infty}^\infty dt H_{\text{int}}(t)\right]|\text{vac}\rangle$$
$$= |\text{vac}\rangle - \frac{i}{\hbar}\int_{-\infty}^\infty dt H_{\text{int}}(t)|\text{vac}\rangle. \tag{17}$$

Inserting Eqs. (3), (5), and (15) into Eq. (17), $|\psi\rangle_{s,\beta,i,\gamma}^{\text{out}}$ can be expressed as

$$|\psi\rangle_{s,\beta,i,\gamma}^{\text{out}} = |\text{vac}\rangle - \frac{i}{\hbar}\varepsilon_0 B\sqrt{2\pi}2\pi\int_0^\infty d\omega_s \int_0^\infty d\omega_i \chi^{(2)}:$$
$$\times \sum_{mn,\,ot,\,rs} \delta(k_{pmnx} - k_{sotx} - k_{irsx})\delta(k_{pmny} - k_{soty} - k_{irsy})$$
$$\times \sum_{w=pF,\,pB}\sum_{g=sF,\,sB}\sum_{h=iF,\,iB} d_w G_{sot}^* G_{irs}^* E_{wmn}\hat{a}_{got}^{2+}\hat{a}_{hrs}^{2+}$$
$$\times \exp[(\beta_{wmn} - \beta_{got}^* - \beta_{hrs}^*)d_w/2]$$
$$\times \text{sinc}[(\beta_{wmn} - \beta_{got}^* - \beta_{hrs}^*)d/2]\delta(\omega_p - \omega_s - \omega_i)|\text{vac}\rangle. \tag{18}$$

Here and in the following, we assume that $\beta_{\varsigma Fmn} = \beta_{\varsigma mn}$ and $\beta_{\varsigma Bmn} = -\beta_{\varsigma mn}$ ($\varsigma = p, s, i$). From Eq. (18), the following relation is satisfied in this process of parametric down-conversion:

$$\omega_p = \omega_s + \omega_i. \tag{19}$$

We are interested only in the second term of $|\psi\rangle_{s,\beta,i,\gamma}^{\text{out}}$ and the first term, vacuum state $|\text{vac}\rangle$, can be neglected. Substituting Eq. (9) into Eq. (18), we can express operators $\hat{a}_{vF}^2$ and $\hat{a}_{vB}^2$ in terms of operators $\hat{a}_{vF}^4$ and $\hat{a}_{vB}^0$. Then the second term $|\psi\rangle_{s,\beta,i,\gamma}^{(2)}$ of $|\psi\rangle_{s,\beta,i,\gamma}^{\text{out}}$ can be divided into the following four parts:

$$|\psi\rangle_{s,\beta,i,\gamma}^{(2)} = |\psi_{s,\beta,i,\gamma}^{FF}\rangle + |\psi_{s,\beta,i,\gamma}^{FB}\rangle + |\psi_{s,\beta,i,\gamma}^{BF}\rangle + |\psi_{s,\beta,i,\gamma}^{BB}\rangle, \tag{20}$$

where

$$|\psi_{s,\beta,i,\gamma}^{FF}\rangle = \int_0^\infty d\omega_s \int_0^\infty d\omega_i [\phi^{FF}(\omega_s, \omega_i)\hat{a}_{sF00,\beta}^{4+}(\omega_s)$$
$$\times \hat{a}_{iF00,\gamma}^{4+}(\omega_i)\delta(\omega_p - \omega_s - \omega_i)]|\text{vac}\rangle, \tag{21a}$$

$$|\psi_{s,\beta,i,\gamma}^{FB}\rangle = \int_0^\infty d\omega_s \int_0^\infty d\omega_i [\phi^{FB}(\omega_s, \omega_i)\hat{a}_{sF00,\beta}^{4+}(\omega_s)$$
$$\times \hat{a}_{iF00,\gamma}^{0+}(\omega_i)\delta(\omega_p - \omega_s - \omega_i)]|\text{vac}\rangle, \tag{21b}$$

$$|\psi_{s,\beta,i,\gamma}^{BF}\rangle = \int_0^\infty d\omega_s \int_0^\infty d\omega_i [\phi^{BF}(\omega_s, \omega_i)\hat{a}_{sF00,\beta}^{0+}(\omega_s)$$
$$\times \hat{a}_{iF00,\gamma}^{4+}(\omega_i)\delta(\omega_p - \omega_s - \omega_i)]|\text{vac}\rangle, \tag{21c}$$

$$|\psi_{s,\beta,i,\gamma}^{BB}\rangle = \int_0^\infty d\omega_s \int_0^\infty d\omega_i [\phi^{BB}(\omega_s, \omega_i)\hat{a}_{sF00,\beta}^{0+}(\omega_s)$$
$$\times \hat{a}_{iF00,\gamma}^{0+}(\omega_i)\delta(\omega_p - \omega_s - \omega_i)]|\text{vac}\rangle, \tag{21d}$$

with

$$\phi^{FF}(\omega_s, \omega_i)$$

$$= -\frac{i}{\hbar} \varepsilon_0 B \sqrt{2\pi} 2\pi \chi^{(2)} : \sum_{mn, ot, rs} \delta(k_{pmnx} - k_{sotx} - k_{irsx})$$

$$\times \delta(k_{pmny} - k_{soty} - k_{irsy}) \exp[(\beta_{wmn} - \beta_{got}^* - \beta_{hrs}^*) d_w/2]$$

$$\times \sum_{\substack{w=pF \\ w=pB}} \sum_{\substack{g=sF(b=11) \\ g=sB(b=21)}} \sum_{\substack{h=iF(c=11) \\ h=iB(c=21)}} d_w \times G_{sot}^* G_{irs}^* E_{wmn}(Fsb)_{ot,00}^* (Fic)_{rs,00}^*$$

$$\times \mathrm{sinc}[(\beta_{wmn} - \beta_{got}^* - \beta_{hrs}^*) d_w/2], \tag{22a}$$

$$\phi^{FB}(\omega_s, \omega_i)$$

$$= -\frac{i}{\hbar} \varepsilon_0 B \sqrt{2\pi} 2\pi \chi^{(2)} : \sum_{mn, ot, rs} \delta(k_{pmnx} - k_{sotx} - k_{irsx})$$

$$\times \delta(k_{pmny} - k_{soty} - k_{irsy}) \exp[(\beta_{wmn} - \beta_{got}^* - \beta_{hrs}^*) d_w/2]$$

$$\times \sum_{\substack{w=pF \\ w=pB}} \sum_{\substack{g=sF(b=11) \\ g=sB(b=21)}} \sum_{\substack{h=iF(c=12) \\ h=iB(c=22)}} d_w \times G_{sot}^* G_{irs}^* E_{wmn}(Fsb)_{ot,00}^* (Fic)_{rs,00}^*$$

$$\times \mathrm{sinc}[(\beta_{wmn} - \beta_{got}^* - \beta_{hrs}^*) d_w/2], \tag{22b}$$

$$\phi^{BF}(\omega_s, \omega_i)$$

$$= -\frac{i}{\hbar} \varepsilon_0 B \sqrt{2\pi} 2\pi \chi^{(2)} : \sum_{mn, ot, rs} \delta(k_{pmnx} - k_{sotx} - k_{irsx})$$

$$\times \delta(k_{pmny} - k_{soty} - k_{irsy}) \exp[(\beta_{wmn} - \beta_{got}^* - \beta_{hrs}^*) d_w/2]$$

$$\times \sum_{\substack{w=pF \\ w=pB}} \sum_{\substack{g=sF(b=12) \\ g=sB(b=22)}} \sum_{\substack{h=iF(c=11) \\ h=iB(c=21)}} d_w \times G_{sot}^* G_{irs}^* E_{wmn}(Fsb)_{ot,00}^* (Fic)_{rs,00}^*$$

$$\times \mathrm{sinc}[(\beta_{wmn} - \beta_{got}^* - \beta_{hrs}^*) d_w/2], \tag{22c}$$

$$\phi^{BB}(\omega_s, \omega_i)$$

$$= -\frac{i}{\hbar} \varepsilon_0 B \sqrt{2\pi} 2\pi \chi^{(2)} : \sum_{mn, ot, rs} \delta(k_{pmnx} - k_{sotx} - k_{irsx})$$

$$\times \delta(k_{pmny} - k_{soty} - k_{irsy}) \exp[(\beta_{wmn} - \beta_{got}^* - \beta_{hrs}^*) d_w/2]$$

$$\times \sum_{\substack{w=pF \\ w=pB}} \sum_{\substack{g=sF(b=12) \\ g=sB(b=22)}} \sum_{\substack{h=iF(c=12) \\ h=iB(c=22)}} d_w \times G_{sot}^* G_{irs}^* E_{wmn}(Fsb)_{ot,00}^* (Fic)_{rs,00}^*,$$

$$\times \mathrm{sinc}[(\beta_{wmn} - \beta_{got}^* - \beta_{hrs}^*) d_w/2], \tag{22d}$$

where $\phi^{FF}(\omega_s, \omega_i)$ represents the probability amplitude that a photon pair occurs signal-forward and idler-forward, $\phi^{FB}(\omega_s, \omega_i)$ corresponds to signal-forward and idler-backward, $\phi^{BF}(\omega_s, \omega_i)$ to signal-backward and idler-forward, and $\phi^{BB}(\omega_s, \omega_i)$ to signal-backward and idler-backward. Here, forward and backward mean that the waves propagate down and up, respectively; the superscripts FF, FB, BF, and BB represent the marks for four kinds of modes, respectively. We only consider the contribution of the special terms $\hat{a}_{vF00,\alpha}^4$ and $\hat{a}_{vB00,\alpha}^0$ of the operator matrixes $\hat{a}_{vF}^4$ and $\hat{a}_{vB}^0$ ($\nu = s, i$) to the probability amplitudes, because these terms correspond to the photons radiated from the three-layer structure without decay. Then $|\phi^{hk}(\omega_s, \omega_i)|^2$ ($h = F, B$, $k = F, B$) can be expressed as

$$|\phi^{hk}(\omega_s, \omega_i)|^2 = f(\omega_s, \omega_i) \delta^2(\omega_p - \omega_s - \omega_i)$$

$$= \lim_{T \to \infty} \frac{2T}{2\pi} f(\omega_s, \omega_i) \delta(\omega_p - \omega_s - \omega_i), \tag{23}$$

with

$$f(\omega_s, \omega_i) = (2\pi)^{3/2} \left(\frac{\varepsilon_0 B}{\hbar c}\right)^2 |\phi(\omega_s, \omega_i)|^2 \tag{24}$$

and

$$\phi(\omega_s, \omega_i) = \sum_{mn, ot, rs} \chi^{(2)} : \exp[(\beta_{wmn} - \beta_{got}^* - \beta_{hrs}^*) d_w/2]$$

$$\times \sum_{\substack{w=pF \\ w=pB}} \sum_{\substack{g=sF(b=hp) \\ g=sB(b=hq)}} \sum_{\substack{h=iF(c=kp) \\ h=iB(c=kq)}} d_w \times G_{sot}^* G_{irs}^* E_{wmn}(Fsb)_{ot,00}^* (Fic)_{rs,00}^*$$

$$(Fp = 11, Fq = 21, Bp = 12, Bq = 22), \tag{25}$$

where the period of nonlinear interaction goes from $-T$ to T. The expressions for the above physical quantities must be normalized by $2T$, which indicates that $2T/2\pi$ will be replaced by $1/2\pi$ in the calculation.

After the output states are obtained, the generation rate of correlated photon pairs can be analyzed. Thus, we define a quantity $N_{s,i}^{hk}(\omega_s, \omega_i)$ that describes the number of photon pairs that have a signal photon at the frequency ω_s and its twin idler photon at the frequency ω_i in the mode hk as follows:

$$N_{s,i}^{hk}(\omega_s, \omega_i) = \langle \psi_{s,\beta,i,\gamma}^{hk} | \hat{n}_{sh,\beta}(\omega_s) \hat{n}_{ik,\gamma}(\omega_i) | \psi_{s,\beta,i,\gamma}^{hk} \rangle, \tag{26}$$

where the density operators of photons $\hat{n}_{sh,\beta}(\omega_s)$ and $\hat{n}_{ik,\gamma}(\omega_i)$ are defined as

$$\hat{n}_{sh,\alpha}(\omega_s) = \hat{a}_{sh00,\alpha}^\dagger \hat{a}_{sh00,\alpha}, \tag{27a}$$

$$\hat{n}_{ik,\alpha}(\omega_i) = \hat{a}_{ik00,\alpha}^\dagger \hat{a}_{ik00,\alpha}, \tag{27b}$$

with

$$\hat{a}_{gF00,\alpha} = \hat{a}_{gF00,\alpha}^4, \tag{28a}$$

$$\hat{a}_{gB00,\alpha} = \hat{a}_{gB00,\alpha}^0, \qquad g = s, i. \tag{28b}$$

Combining Eqs. (21) and (23), the quantity $N_{s,i}^{hk}(\omega_s, \omega_i)$ can be written as

$$N_{s,i}^{hk}(\omega_s, \omega_i) = |\phi^{hk}(\omega_s, \omega_i)|^2. \tag{29}$$

Then we introduce $N_s^{hk}(\omega_s)$ to describe the number of signal photons at the frequency ω_s in the mode hk; it can be expressed in the following form:

$$N_s^{hk}(\omega_s) = \int_0^\infty d\omega_i |\phi^{hk}(\omega_s, \omega_i)|^2. \tag{30}$$

Sometimes, the energy spectrum of the signal field $S_s^{h,k}(\omega_s)$ is easy to be measured from the experimental view and is determined by the following expression:

$$S_s^{h,k}(\omega_s) = \hbar\omega_s N_s^{h,k}(\omega_s) = \hbar\omega_s \int_0^\infty d\omega_i |\phi^{hk}(\omega_s, \omega_i)|^2. \tag{31}$$

Inserting Eq. (23) into Eqs. (30) and (31), $N_s^{hk}(\omega_s)$ and $S_s^{h,k}(\omega_s)$ can be expressed as

$$N_s^{b,k}(\omega_s) = \frac{1}{2\pi} f[\omega_s, (\omega_p - \omega_s)], \qquad \text{(32)}$$

$$S_s^{b,k}(\omega_s) = \frac{\hbar\omega_s}{2\pi} f[\omega_s, (\omega_p - \omega_s)]. \qquad \text{(33)}$$

Based on Eqs. (32) and (33), the mean number of photon pairs and the energy spectrum of the signal field can be obtained easily by the numerical calculations.

3. RESULTS AND DISCUSSION

In this section, we present numerical results for the efficiency of the photon-pair generation from the three-layer structure. In the following calculations, we take silicon nitride Si_3N_4 as a component of the photonic crystal slab and ZnSe as the material of the dielectric slab; their relative permittivities are taken as $\varepsilon_p = 4.0$ and $\varepsilon_s = 6.0516$ [49]. The second-order nonlinear susceptibility of the monolayer WS_2 is chosen to be $\chi^{(2)} = 100$ pm/V, which is compatible with the results in Ref. [50], and the second nonlinear effects of Si_3N_4 and ZnSe can be neglected. We choose WS_2 as the two-dimensional material because of its large second nonlinear susceptibility [42].

Figures 2(a)–2(c) show the transmission (t), reflection (r), and absorption (a) for the three-layer structure as a function of the wavelength; Figures 2(d)–2(f) correspond to the transmission (t'), reflection (r'), and absorption (a') for the same structure, respectively. The parameters are assumed to be the following: $r = 0.2l$, $d_1 = 1.0l$, $d_2 = 1.7l$, and $l = 700$ nm, and the angle of the incident electromagnetic wave is taken as 0°.
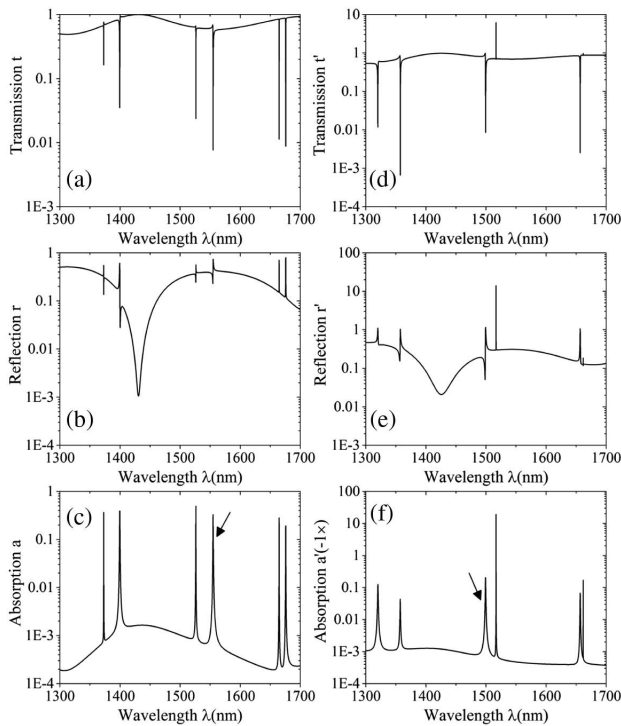
It is clearly seen that many sharp resonant peaks appear, which correspond to BICs. The spectra on the left do not coincide with those on the right. The phenomenon originates from the non-Hermitian characteristics of the structure due to the losses of absorption and radiation [4]. The energy conservation law $t + r + a = 1$ is satisfied for the t, r, and a, which are determined by the scattering matrix Q. The corresponding energy conservation law $t' + r' + a' = 1$ is also satisfied for t', r', and a', which are obtained by the inverse scattering matrix Q^{-1*}. The t, r, and a vary between 0 and 1, but t' and r' may be greater than 1 and a' may be less than –1. This is because the inverse scattering matrix Q^{-1*} describes the electromagnetic field being radiated from the three-layer structure, whereas the scattering matrix Q represents the electromagnetic field being absorbed by the structure.

In the following, we study the effect of the BIC on the second-harmonic generation (SHG) and photon-pair generation from the designed three-layer structure. As shown in Figs. 2(c) and 2(f) by the arrows, we take one BIC determined by the scattering matrix, which is located at 1555.0222 nm, and another BIC determined by the inverse scattering matrix, which is located at 1499.254 nm.

Figures 3(a) and 3(b) display the corresponding SHG conversions as a function of the wavelength of the pump field in different frequency regions. For comparison, the corresponding SHG conversion from the freestanding monolayer WS_2 is represented by dashed lines. The incident angle and intensity of the pump field are taken as 0° and 100 MW/cm². It is seen from Fig. 3(a) that resonant peaks of the downward and upward second-harmonic waves appear and are located at the
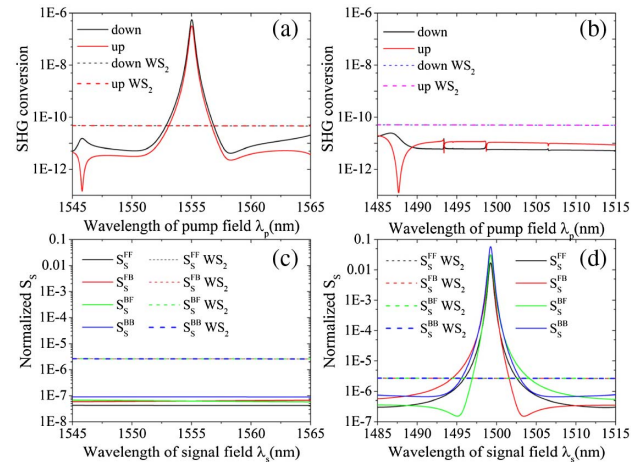

Fig. 2. (a), (b), and (c) show the transmission (t), reflection (r), and absorption (a) spectra for the three-layer structure as shown in Fig. 1, respectively. (d), (e) and (f) display the corresponding transmission (t'), reflection (r'), and absorption (a') spectra, respectively.

Fig. 3. (a) and (b) describe the downward (black line) and upward (red line) SHG conversion from the three-layer structure as a function of the wavelength of the pump field in different regions, and the corresponding SHG conversions from the freestanding monolayer WS_2 are shown by the corresponding dashed lines. (c) and (d) exhibit energy S_s^{FF} (black line), S_s^{FB} (red line), S_s^{BF} (green line), and S_s^{BB} (blue line) of the three-layer structure as a function of the wavelength of the signal field in different regions, the corresponding energy spectra of the freestanding monolayer WS_2 are represented by the dashed lines, and the wavelength of the pump field is $\lambda_p = 749.627$ nm. The parameters are assumed as follows: $d_1 = 1.00l$, $d_2 = 1.70l$, $r = 0.20l$, and $l = 700$ nm.

wavelength $\lambda_p = 1555.0222$ nm, which corresponds to the wavelength of the BIC determined by the scattering matrix. The efficiency of SHG in the monolayer WS$_2$ is enhanced by about 4 orders of magnitude. In contrast, in Fig. 3(b) we cannot observe the resonant peaks near the BIC determined by the inverse scattering matrix.

In Figs. 3(c) and 3(d), we plot energy spectra for S_s^{FF}, S_s^{FB}, S_s^{BF}, and S_s^{BB} of the three-layer structure as a function of the wavelength λ_s of the signal field. The pump field with the intensity 100 MW/cm^2 is incident perpendicularly to the structure ($\theta_p = 0°$), and the angle of the signal field is taken as $\theta_s = 0°$. In order to make sure the signal and idler fields are located at the resonant states simultaneously, the wavelength of the pump field is fixed at $\lambda_p = 749.627$ nm. For comparison, the corresponding energy spectra of the freestanding monolayer WS$_2$ are also shown by the dashed lines. Because of the ultrathin thickness, the downward and upward SHG conversions from the freestanding monolayer are nearly equal, the energy spectra in four modes of the freestanding monolayer WS$_2$ are also nearly equal, and thus the dashed lines almost coincide with each other.

From Fig. 3(c), we can see that there is no resonant peak when the signal field is located at the BIC determined by the scattering matrix. The resonant peaks of energy spectra appear at $\lambda_s = 1499.254$ nm $= 2\lambda_p$ in Fig. 3(d), where the signal field is located at the BIC determined by the inverse scattering matrix. The corresponding wavelength of the idler field is $\lambda_i = \lambda_s$, which is obtained from the energy conservation condition $\omega_p = \omega_s + \omega_i$, and the radiated angle of the idler field is $\theta_i = 0°$, which is determined by the phase-matching condition as shown in Eq. (11), so the idler field is also located at the BIC determined by the inverse scattering matrix. Comparing these results with those from the freestanding monolayer WS$_2$, the energies of the signal field from the three-layer structure are enhanced by about 4 orders of magnitude.

These phenomena are different from some previous studies on the enhancement of photon-pair generation in one-dimensional photonic crystal [12,13,18], which is determined by the scattering matrix Q. As can be seen from Eq. (9), the annihilation operators of the generated fields are closely related to Q^{-1*}, and thus the corresponding creation operators are connected by Q^{-1*}. In Fig. 2, it is shown that the photon-pair generation is enhanced in the parametric down-conversion if the signal and idler fields are located at the BIC determined by the inverse scattering matrix Q^{-1*}. This can be understood by the distributions of the electric field amplitude in the structure.

In Figs. 4(a) and 4(b), we plot the electric field enhancements $|\mathbf{E}_W|$ (black line) and $|\mathbf{E}'_W|$ (red line) determined by the scattering matrix and inverse scattering matrix of the three-layer structure as a function of the wavelength. The strength of the incident electrical field is assumed as 1, and here we neglect the nonlinear effect on the field distribution. It is clearly observed at $\lambda = 1555.0222$ nm that a resonant peak appears for $|\mathbf{E}_W|$, while there is no resonant peak for $|\mathbf{E}'_W|$, so at this location the SHG [Fig. 3(a)] is enhanced. It is also clearly seen at $\lambda = 1499.254$ nm that the resonant peak appears for $|\mathbf{E}'_W|$, while there is no resonant peak for $|\mathbf{E}_W|$, so at this location the efficiency of photon-pair generation
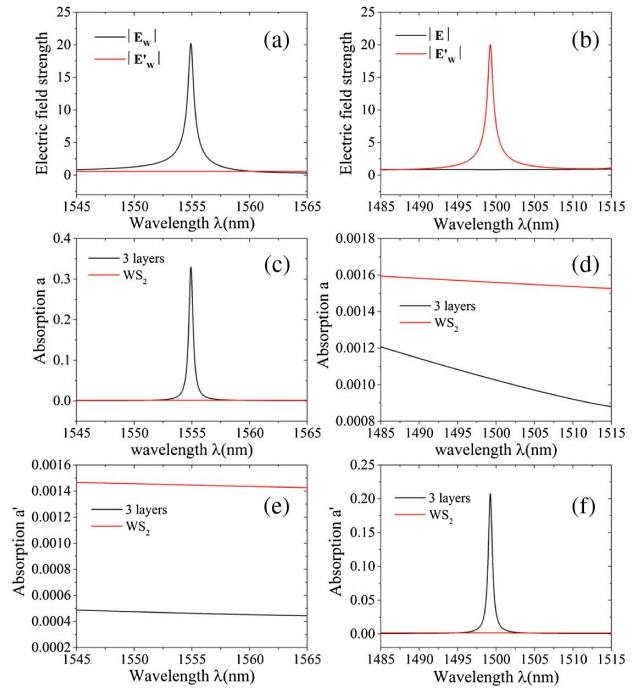

Fig. 4. (a) and (b) exhibit the electric field enhancements $|\mathbf{E}_W|$ (black line) and $|\mathbf{E}'_W|$ (red line) determined by the scattering matrix and inverse scattering matrix of the three-layer structure as a function of the wavelength. (c) and (d) describe the absorption a of the three-layer structure as a function of the wavelength in different regions; the corresponding absorption a of the freestanding monolayer WS$_2$ is shown by the corresponding red lines. (e) and (f) show the absorption a' of the three-layer structure as a function of the wavelength in different regions; the corresponding absorption a' of the freestanding monolayer WS$_2$ is represented by the red lines.

[Fig. 3(d)] is improved. Because the scattering matrix Q is different from the inverse scattering matrix Q^{-1*}, the enhancements $|\mathbf{E}_W|$ and $|\mathbf{E}'_W|$ play different roles in the two processes. The corresponding absorption spectra a (a') in the structure are also shown in Figs. 4(c) and 4(d) [Figs. 4(e) and 4(f)]. It is seen clearly in Figs. 4(c) and 4(f) that there is a resonant peak of absorption a (a'), which originates from the obvious resonant peak of the field $|\mathbf{E}_W|$ ($|\mathbf{E}'_W|$). These phenomena should be attributed to non-Hermitian behavior of the structure due to the losses of absorption and radiation.

In addition to high generation rate, the signals generated in such a way have narrowed relative line width due to the appearance of the BICs [29]. The relative line width can be described by $\Delta\lambda/\lambda_\Gamma$ in the signal spectrum; here λ_Γ is the center wavelength of the peak and $\Delta\lambda$ represents the full width at half-maximum of the peak. For example, $\Delta\lambda/\lambda_\Gamma$ is 0.0181% in Fig. 3(a) and 0.0268% in Fig. 3(d), which is much smaller than the relative line width presented in Ref. [51].

So far, the discussions are only for the case with the incident angle 0° of the pump field. In fact, the above phenomena also depend on the angle of the pump field. Figure 5(b) displays the energy spectra S_s^{FF} of the three-layer structure as a function of λ_s at various radiated angle θ_s; the intensity of the pump field $I_p = 100$ MW/cm^2 and $\theta_p = 0°$ are taken, and the radiated
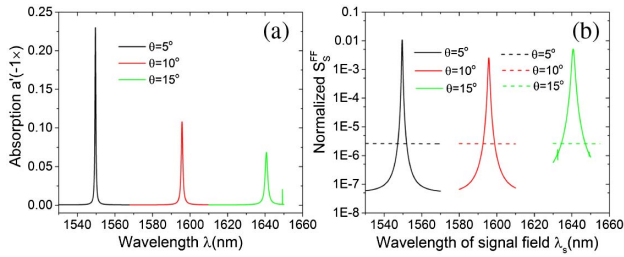
Fig. 5. (a) The absorption a' of the three-layer structure as a function of the wavelength λ at various incident angles; the black, red, and green lines are the spectra at the incident angles $\theta = 5°$, $10°$, and $15°$, respectively. (b) The energy spectra S_s^{FF} of the three-layer structure as a function of the wavelength λ_s at various radiated angles of the signal field $\theta_s = 5°$, $10°$, and $15°$; the corresponding energy spectra of the freestanding monolayer WS$_2$ are denoted by the dashed lines. The wavelengths of the pump fields which are incident normally are taken as $\lambda_p = 774.808$ nm, 797.856 nm, and 820.341 nm for various θ_s, respectively; the other parameters are assumed as follows: $d_1 = 1.00l$, $d_2 = 1.70l$, $r = 0.20l$, and $l = 700$ nm.

Fig. 6. (a) The absorption a' of the three-layer structure as a function of the incident angle θ. (b) The energy spectra S_s^{FF} (black line), S_s^{FB} (red line with circle), S_s^{BF} (green line with triangle), and S_s^{BB} (blue line) of the three-layer structure as a function of the radiated angle θ_s of the signal field. The wavelength of the pump field, which is incident normally, is taken as $\lambda_p = 749.627$ nm, and the wavelengths of the signal and idler fields are fixed at $\lambda_s = \lambda_i = 2\lambda_p = 1499.254$ nm, the other parameters are assumed as follows: $d_1 = 1.00l$, $d_2 = 1.70l$, $r = 0.20l$, and $l = 700$ nm.

angle θ_i is equal to $\theta_i = -\theta_s$ according to the phase matching condition. The wavelength of the pump field is chosen to make sure the signal and idler fields are located at the BICs determined by the inverse scattering matrix simultaneously. For comparison, the corresponding energy spectra of the freestanding monolayer WS$_2$ are provided by the dashed lines. It is clearly seen that the resonant peaks appear at various radiated angles θ_s and are redshifted with the increase of θ_s. The relative line widths of the resonant peaks at the three different angles are 0.02324%, 0.04288%, and 0.06858%, respectively.

This means that narrowed relative line width of the generated signal is observed again. In order to disclose the physical origin of the phenomena, in Fig. 5(a) we plot the corresponding absorption a' of the three-layer structure as a function of the wavelength λ. The resonant peaks in absorption spectra correspond to the resonant peaks of the energy S_s^{FF}. These show again that the photon-pair generation can be enhanced dramatically if the signal and idler fields are located at the BIC simultaneously. The narrowed relative line width of the generated signal can be understood from the narrowed relative line width of absorption a'.

The above phenomena not only depend on the incident angle of the pump field; they are also sensitive to the radiated angle of the signal field. Figure 6(b) describes the energy S_s^{FF}, S_s^{FB}, S_s^{BF}, and S_s^{BB} of the three-layer structure as a function of the radiated angle θ_s, the pump field is incident normally, and the wavelengths of the pump and signal fields are chosen at $\lambda_p = 749.627$ nm and $\lambda_s = 1499.254$ nm corresponding to the maximum in Fig. 3(d). We find that the energy S_s^{FF} decreases dramatically with the increase of the radiated angle θ_s and also nearly arrives at the minimum at 1°; this means that the present structure can be used to generate photon pairs with outstanding directivity. Such a phenomenon also corresponds to the absorption a' of the three-layer structure as a function of the incident angle as shown in Fig. 6(a). This is because the BIC is very sensitive to the incident angle.
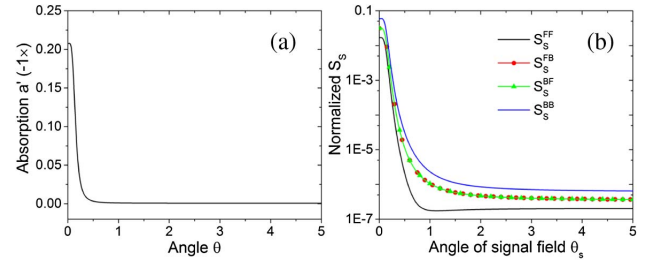
In the following, we provide the calculated results of the energy S_s^{FF} as a function of the wavelength λ_s for different tunable variables of the system. Figure 7 displays these results. Figures 7(a)–7(c) correspond to the cases with various radii of the air hole and the thicknesses of the photonic crystal slab and dielectric slab, respectively. The wavelengths of the pump fields are also taken to make sure the signal and idler fields are located at the BICs determined by the inverse scattering matrix simultaneously. For comparison, the corresponding energy spectra of the freestanding monolayer WS$_2$ are also represented by the dashed lines. The location of the energy peak is blueshifted with the increase of the radius r as shown in Fig. 7(a) and redshifted with the increase of the thickness d_2 of the dielectric slab as shown in Fig. 7(c). The location of the energy peak is nearly unchanged after tuning the thickness d_1 of the photonic crystal slab as shown in Fig. 7(b). The peak value can be tuned by changing the parameters r, d_1, and d_2, and the enhancement arrives at about 7 orders when the radius of the air hole is taken as $r = 0.10l$.

In addition, we would like to point out that the generation rate of correlated photon pairs also depends on the azimuthal angle. Here the azimuthal angle is defined as the angle between the electric field and the x axis when the corresponding electromagnetic wave is incident or radiated normally. In the above calculations, the pump field is polarized along the y direction; that is to say, the azimuthal angle is fixed at $\phi = 90°$, and the polarizations of the signal and idler fields are chosen along the y direction.

Figure 7(d) shows the energy S_s^{FF} for different polarizations of generated photons as a function of the azimuthal angle ϕ of the normal pump field, and the signal and idler fields are also radiated normally. A period modulation in the spectra with period 180° is observed clearly. As ϕ is increased from 0° to 360°, the polarization of the pump electric field is rotated anticlockwise from the x direction back to the original direction, and when the azimuthal angle is taken at $\phi = 0°$, the pump electric field is polarized along the x direction. In such a case, the energies S_s^{FF} resulting from the second-order nonlinear polarization $\chi_{yyy}^{(2)}$ and $\chi_{yxx}^{(2)}$ are the minima, and those resulting from the second-order nonlinear polarization $\chi_{xyx}^{(2)}$ and $\chi_{xxy}^{(2)}$ are
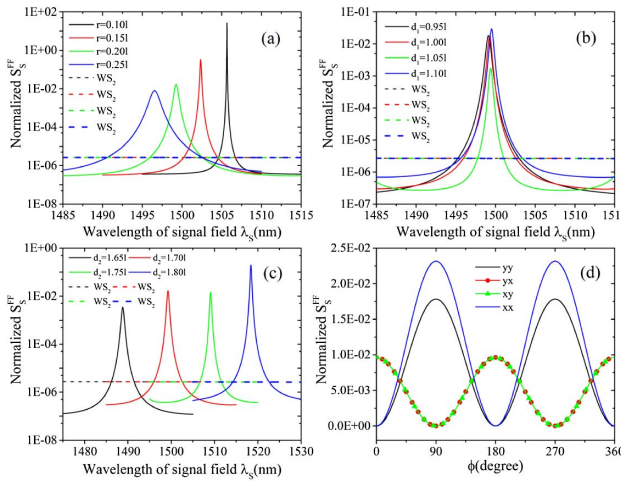
Fig. 7. (a), (b), and (c) The energy S_s^{FF} as a function of the wavelength of the signal field under normal incident pump field, the signal and idler fields are also radiated normally, and the corresponding spectra of the freestanding monolayer WS_2 are described by the dashed lines. (a) Various radii of the air hole; the wavelengths of the pump fields are fixed at $\lambda_p = 752.828$ nm, 751.173 nm, 749.627 nm, and 748.271 nm when the radii are $r = 0.01l$, 0.15l, 0.20l, and 0.25l. The other parameters are taken as follows: $d_1 = 1.00l$ and $d_2 = 1.70l$. (b) Various thicknesses of the photonic crystal slab; the wavelengths of the pump fields are fixed at $\lambda_p = 749.551$ nm, 749.627 nm, 749.694 nm, and 749.749 nm when the thicknesses are $d_1 = 0.95l$, 1.00l, 1.05l, and 1.10l. The other parameters are taken as follows: $d_2 = 1.70l$ and $r = 0.20l$. (c) Various thicknesses of the dielectric slab; the wavelengths of the pump fields are fixed at $\lambda_p = 744.405$ nm, 749.627 nm, 754.555 nm, and 759.204 nm when the thicknesses are $d_2 = 1.65l$, 1.70l, 1.75l, and 1.80l. The other parameters are taken as follows: $d_1 = 1.00l$ and $r = 0.20l$. (d) The energy S_s^{FF} for different polarizations of generated photons as a function of the azimuthal angle of the normal incident pump field; the signal and idler fields are also radiated normally and are polarized in the yy, yx, xy, xx directions. The parameters are assumed as follows: $d_1 = 1.00l$, $d_2 = 1.70l$, $r = 0.20l$, and $\lambda_s = \lambda_i = 2\lambda_p = 1499.254$ nm.

the maxima. Thus, the generation efficiencies of signal and idler fields with polarizations yy and xx reach the minima, and those with polarizations yx and xy reach the maxima. The corresponding phenomena can also be found for the case with the azimuthal angle $\phi = 90°$. This means that we can also utilize this property to tune the generation rate of the correlated photon pairs in a large range by changing the azimuthal angle.

4. SUMMARY

In summary, we have designed the photonic crystal slab-WS_2-slab structures to improve the generation rate of correlated photon pairs. In order to calculate the generation rate of correlated photon pairs in such structures, the rigorous quantum theory of spontaneous parametric down-conversion with the plane wave expansion method has been developed. The mean number of output photon pairs and the signal field energy spectra have been calculated. The BIC of radiation modes in the monolayer WS_2 has been demonstrated. We have found that the generation efficiency of correlated photon pairs is greatly improved

if the signal and idler fields are located at the BIC determined by the inverse scattering matrix of the structure. This is in contrast to the previous investigations on the enhancement of photon-pair generation in some nanostructures such as photonic crystals, which is determined by the scattering matrix. The effect of the structure parameters on the generation rate of correlated photon pairs has also been discussed. It is found that the generation rate of the correlated photon pair can be improved by 7 orders of magnitude in some designed structures. The generated quantum signals are sensitive to the wavelength and exhibit narrowed relative line width and directivity, which is very beneficial for the quantum information processing.

REFERENCES

1. D. Bouwmeester, A. Ekert, and A. Zeilinger, *The Physics of Quantum Information* (Springer, 2000).
2. M. A. Nielsen and I. L. Chuang, *Quantum Computation and Quantum Information* (Cambridge University, 2000).
3. E. Knill, R. Laflamme, and G. J. Milburn, "A scheme for efficient quantum computation with linear optics," Nature (London) **409**, 46–52 (2001).
4. C. Janisch, Y. Wang, D. Ma, N. Mehta, A. L. Elías, N. Perea-López, M. Terrones, V. Crespi, and Z. Liu, "Extraordinary second harmonic generation in tungsten disulfide monolayers," Sci. Rep. **4**, 5530 (2014).
5. L. M. Malard, T. V. Alencar, A. P. M. Barboza, K. F. Mak, and A. M. de Paula, "Observation of intense second harmonic generation from MoS_2 atomic crystals," Phys. Rev. B **87**, 201401 (2013).
6. A. N. Vamivakas, B. E. A. Saleh, A. V. Sergienko, and M. C. Teich, "Quantum ellipsometry using correlated-photon beams," Phys. Rev. A **70**, 043810 (2004).
7. Y. Zeng, Y. Fu, X. Chen, W. Lu, and H. Agren, "Highly efficient generation of entangled photon pair by spontaneous parametric down-conversion in defective photonic crystals," J. Opt. Soc. Am. B **24**, 1365–1368 (2007).
8. P. G. Kwiat, K. Mattle, H. Weinfurter, A. Zeilinger, A. V. Sergienko, and Y. Shih, "New high-intensity source of polarization-entangled photon pairs," Phys. Rev. Lett. **75**, 4337–4341 (1995).
9. X. H. Bao, Y. Qian, J. Qian, J. Yang, H. Zhang, Z. B. Chen, T. Yang, and J. W. Pan, "Generation of narrow-band polarization entangled photon pairs for atomic quantum memories," Phys. Rev. Lett. **101**, 190501 (2008).
10. K. Niizeki, K. Ikeda, M. D. Zheng, X. P. Xie, K. Okamura, N. Takei, N. Namekata, S. Inoue, H. Kosaka, and T. Y. Horikiri, "Ultrabright narrow-band telecom two-photon source for long-distance quantum communication," Appl. Phys. Express **11**, 042801 (2018).
11. D. Huber, M. Reindl, J. Aberl, A. Rastelli, and R. Trotta, "Semiconductor quantum dots as an ideal source of polarization entangled photon pairs on-demand: a review," J. Opt. **20**, 073002 (2018).
12. M. J. A. de Dood, W. T. M. Irvine, and D. Bouwmeester, "Nonlinear photonic crystals as a source of entangled photons," Phys. Rev. Lett. **93**, 040504 (2004).
13. W. T. M. Irvine, M. J. A. de Dood, and D. Bouwmeester, "Bloch theory of entangled photon generation in non-linear photonic crystals," Phys. Rev. A **72**, 043815 (2005).
14. M. Centini, J. Perina, Jr., L. Sciscione, C. Sibilia, M. Scalora, M. J. Bloemer, and M. Bertolotti, "Entangled photon pair generation by spontaneous parametric down-conversion in finite-length one-dimensional photonic crystals," Phys. Rev. A **72**, 033806 (2005).
15. L. Sciscione, M. Centini, C. Sibilia, M. Bertolotti, and M. Scalora, "Entangled, guided photon generation in (1+1)-dimensional photonic crystals," Phys. Rev. A **74**, 013815 (2006).

16. V. Roppo, M. Centini, C. Sibilia, M. Bertolotti, D. de Ceglia, M. Scalora, N. Akozbek, M. J. Bloemer, J. W. Haus, O. G. Kosareva, and V. P. Kandidov, "Role of phase matching in pulsed second-harmonic generation: walk-off and phase-locked twin pulses in negative-index media," Phys. Rev. A **76**, 033829 (2007).

17. X. Li, P. L. Voss, J. E. Sharping, and P. Kumar, "Optical-fiber source of polarization-entangled photons in the 1550 nm telecom band," Phys. Rev. Lett. **94**, 053601 (2005).

18. J. G. Rarity, J. Fulconis, J. Duligall, W. J. Wadsworth, and P. S. Russell, "Photonic crystal fiber source of correlated photon pairs," Opt. Express **13**, 534–544 (2005).

19. J. Fulconis, O. Alibart, W. J. Wadsworth, P. S. Russell, and J. G. Rarity, "High brightness single mode source of correlated photon pairs using a photonic crystal fiber," Opt. Express **13**, 7572–7582 (2005).

20. S. Wei, Y. Dong, H. Wang, and X. D. Zhang, "Enhancement of correlated photon-pair generation from a positive-negative index material heterostructure," Phy. Rev. A **81**, 053830 (2010).

21. Y. Li, Y. Rao, K. F. Mak, Y. You, S. Wang, C. R. Dean, and T. F. Heinz, "Probing symmetry properties of few-layer MoS_2 and h-BN by optical second-harmonic generation," Nano Lett. **13**, 3329–3333 (2013).

22. K. L. Seyler, J. R. Schaibley, P. Gong, P. Rivera, A. M. Jones, S. Wu, J. Yan, D. G. Mandrus, W. Yao, and X. Xu, "Electrical control of second-harmonic generation in a WSe_2 monolayer transistor," Nat. Nanotechnol. **10**, 407–411 (2015).

23. M. Weismann and N. C. Panoiu, "Theoretical and computational analysis of second- and third-harmonic generation in periodically patterned graphene and transition monolayers," Phys. Rev. B **94**, 035435 (2016).

24. M. A. Vincenti, D. de Ceglia, M. Grande, A. D'Orazio, and M. Scalora, "Nonlinear processes in one-dimensional photonic crystal with graphene-based defect," Phys. Rev. B **89**, 165139 (2014).

25. S. Zhang and X. D. Zhang, "Strong second-harmonic generation from bilayer-graphene embedded in one-dimensional photonic crystals," J. Opt. Soc. Am. B **33**, 452–460 (2016).

26. J. Niu, M. Luo, and Q. H. Liu, "Enhancement of graphene's third-harmonic generation with localized surface plasmon resonance under optical/electro-optic Kerr effects," J. Opt. Soc. Am. B **33**, 615–621 (2016).

27. L. Wang, T. Wang, S. Zhang, P. Xie, and X. D. Zhang, "Larger enhancement in four-wave mixing from graphene embedded in one-dimensional photonic crystals," J. Opt. Soc. Am. B **34**, 2000–2010 (2017).

28. M. Zhang and X. D. Zhang, "Ultrasensitive optical absorption in graphene based on bound states in the continuum," Sci. Rep. **5**, 8266 (2015).

29. A. Kodigala, T. Lepetit, Q. Gu, B. Bahari, Y. Fainman, and B. Kanté, "Lasing action from photonic bound states in continuum," Nature **541**, 196–199 (2017).

30. D. C. Marinica, A. G. Borisov, and S. V. Shabanov, "Bound states in continuum in photonics," Phys. Rev. Lett. **100**, 183902 (2008).

31. E. N. Bulgakov and A. F. Sadreev, "Bound states in the continuum in photonic waveguides inspired by defects," Phys. Rev. B **78**, 075105 (2008).

32. Y. Plotnik, O. Peleg, F. Dreisow, M. Heinrich, S. Nolte, A. Szameit, and M. Segev, "Experimental observation of optical bound states in the continuum," Phys. Rev. Lett. **107**, 183901 (2011).

33. M. I. Molina, A. E. Miroshnichenko, and Y. S. Kivshar, "Surface bound states in the continuum," Phys. Rev. Lett. **108**, 070401 (2012).

34. J. Lee, B. Zhen, S. L. Chua, W. Qiu, J. D. Joannopoulos, M. Soljačić, and O. Shapira, "Observation and differentiation of unique high-Q optical resonances near zero wave vector in macroscopic photonic crystal slabs," Phys. Rev. Lett. **109**, 067401 (2012).

35. C. W. Hsu, B. Zhen, J. Lee, S. L. Chua, S. G. Johnson, J. D. Joannopoulos, and M. Soljačić, "Observation of trapped light within the radiation continuum," Nature **499**, 188–191 (2013).

36. C. W. Hsu, B. Zhen, S. L. Chua, S. G. Johnson, J. D. Joannopoulos, and M. Soljačić, "Bloch surface eigenstates within the radiation continuum," Light Sci. Appl. **2**, e84 (2013).

37. F. Monticone and A. Alù, "Embedded photonic eigenvalues in 3D nanostructures," Phys. Rev. Lett. **112**, 213903 (2014).

38. B. Zhen, C. W. Hsu, L. Lu, A. D. Stone, and M. Soljačić, "Topological nature of optical bound states in the continuum," Phys. Rev. Lett. **113**, 257401 (2014).

39. M. G. Silveirinha, "Spontaneous parity-time-symmetry breaking in moving media," Phys. Rev. A **89**, 023813 (2014).

40. E. N. Bulgakov, K. N. Pichugin, and A. F. Sadreev, "All-optical light storage in bound states in the continuum and release by demand," Opt. Express **23**, 22520–22531 (2015).

41. T. Wang and X. D. Zhang, "Improved third-order nonlinear effect in graphene based on bound states in the continuum," Photon. Res. **5**, 629–639 (2017).

42. Y. Li, A. Chernikov, X. Zhang, A. Rigosi, H. M. Hill, A. M. van der Zande, D. A. Chenet, E.-M. Shih, J. Hone, and T. F. Heinz, "Measurement of the optical dielectric function of monolayer transition-metal dichalcogenides MoS_2, $MoSe_2$, WS_2, and WSe_2," Phys. Rev. B **90**, 205422 (2014).

43. M. Weismann and N. C. Panoiu, "Theoretical and computational analysis of second-and third-harmonic generation in periodically patterned graphene and transition-metal dichalcogenide monolayers," Phys. Rev. B **94**, 035435 (2016).

44. Y. Yang, C. Peng, Y. Liang, Z. Li, and S. Noda, "Analytical perspective for bound states in the continuum in photonic crystal slabs," Phys. Rev. Lett. **113**, 037401 (2014).

45. Z. Y. Li and L. L. Lin, "Photonic band structures solved by a plane-wave-bases transfer-matrix method," Phys. Rev. E **67**, 046607 (2003).

46. T. Gruner and D.-G. Welsh, "Green-function approach to the radiation-field quantization for homogeneous and inhomogeneous Kramers-Kronig dielectrics," Phys. Rev. A **53**, 1818–1829 (1996).

47. N. Stefanou, V. Yannopapas, and A. Modinos, "Heterostructures of photonic crystals: frequency bands and transmission coefficients," Comput. Phys. Commun. **113**, 49–77 (1998).

48. T. R. Zhan, X. Shi, Y. Y. Dai, X. H. Liu, and J. Zi, "Transfer matrix method for optics in graphene layers," J. Phys. Condens. Matter **25**, 215301 (2013).

49. E. D. Palik and G. Ghosh, *Handbook of Optical Constants of Solids* (Academic, 1998).

50. E. N. Bulgakov and A. F. Sadreev, "Transfer of spin angular momentum of an incident wave into orbital angular momentum of the bound states in the continuum in an array of dielectric spheres," Phys. Rev. A **94**, 033856 (2016).

51. A. Aryshev, A. Potylitsyn, G. Naumenko, M. Shevelev, K. Lekomtsev, L. Sukhikh, P. Karataev, Y. Honda, N. Terunuma, and J. Urakawa, "Monochromaticity of coherent Smith-Purcell radiation from finite size grating," Phys. Rev. Beams **20**, 024701 (2017).